

Non-trivial band topology and orbital-selective electronic nematicity in a titanium-based kagome superconductor

Received: 12 January 2023

Accepted: 18 August 2023

Published online: 21 September 2023

 Check for updates

Yong Hu ^{1,10} , Congcong Le ^{2,10}, Yuhang Zhang ^{3,4,10}, Zhen Zhao^{3,4}, Jiali Liu^{3,4}, Junzhang Ma ^{5,6}, Nicholas C. Plumb ¹, Milan Radovic ¹, Hui Chen ^{3,4}, Andreas P. Schnyder ⁷, Xianxin Wu ⁸ , Xiaoli Dong ^{3,4}, Jiangping Hu ^{3,4}, Haitao Yang ^{3,4}, Hong-Jun Gao ^{3,4}  & Ming Shi ^{1,9} 

Electronic nematicity that spontaneously breaks rotational symmetry is a generic phenomenon in correlated quantum systems including high-temperature superconductors and the AV_3Sb_5 (A can be K, Rb or Cs) family of kagome superconductors. However, the underlying mechanism of nematicity in these systems is hard to identify because of its entanglement with other ordered phases. Recently, a family of titanium-based kagome superconductors ATi_3Bi_5 have been synthesized, where electronic nematicity occurs in the absence of charge order. It provides a platform to study nematicity in its pure form, as well as its interplay with orbital degrees of freedom. Here we reveal the band topology and orbital characters of the multiorbital $RbTi_3Bi_5$. We use polarization-dependent angle-resolved photoemission spectroscopy with density functional theory to identify the coexistence of flat bands, type-II Dirac nodal lines and non-trivial topology in this compound. Our study demonstrates the change in orbital character along the Fermi surface contributed by the kagome bands, implying a strong intrinsic interorbital coupling in the Ti-based kagome metals. Furthermore, doping-dependent measurements uncover the orbital-selective features in the kagome bands, which can be explained by d - p hybridization. Hence, interorbital coupling together with d - p hybridization is probably the origin of electronic nematicity in ATi_3Bi_5 .

Electronic nematicity and its fluctuations, which are present in numerous strongly correlated materials^{1–9}, are arguably linked to emergent superconductivity. However, understanding the underlying driving force behind electronic nematicity remains a central challenge in the study of correlated quantum systems. In the case of iron-based superconductors, the resolution of this question is complicated by the convoluted interplay between spin, orbital and lattice degrees of freedom¹⁰. Similarly, in the cuprate high-temperature superconductors, the entanglement of nematicity with charge (density wave)

order poses difficulties in unravelling its origin¹¹. The kagome lattice—a corner-sharing triangle network—has emerged as one of the most fundamental systems for investigating exotic correlated and topological quantum states. Due to its frustrated lattice geometry and unique correlation effects embedded in flat bands and Van Hove singularities^{12–19}, a wide range of electronic instabilities and non-trivial topologies have been observed, including quantum spin liquid^{20–23}, Dirac/Weyl semimetals^{24–26}, charge density wave (CDW) orders^{12–14} and unconventional superconductivity^{12–14,27}. Within this realm,

A full list of affiliations appears at the end of the paper.  e-mail: yonghphysics@gmail.com; xxwu@itp.ac.cn; hjgao@iphy.ac.cn; ming.shi@psi.ch

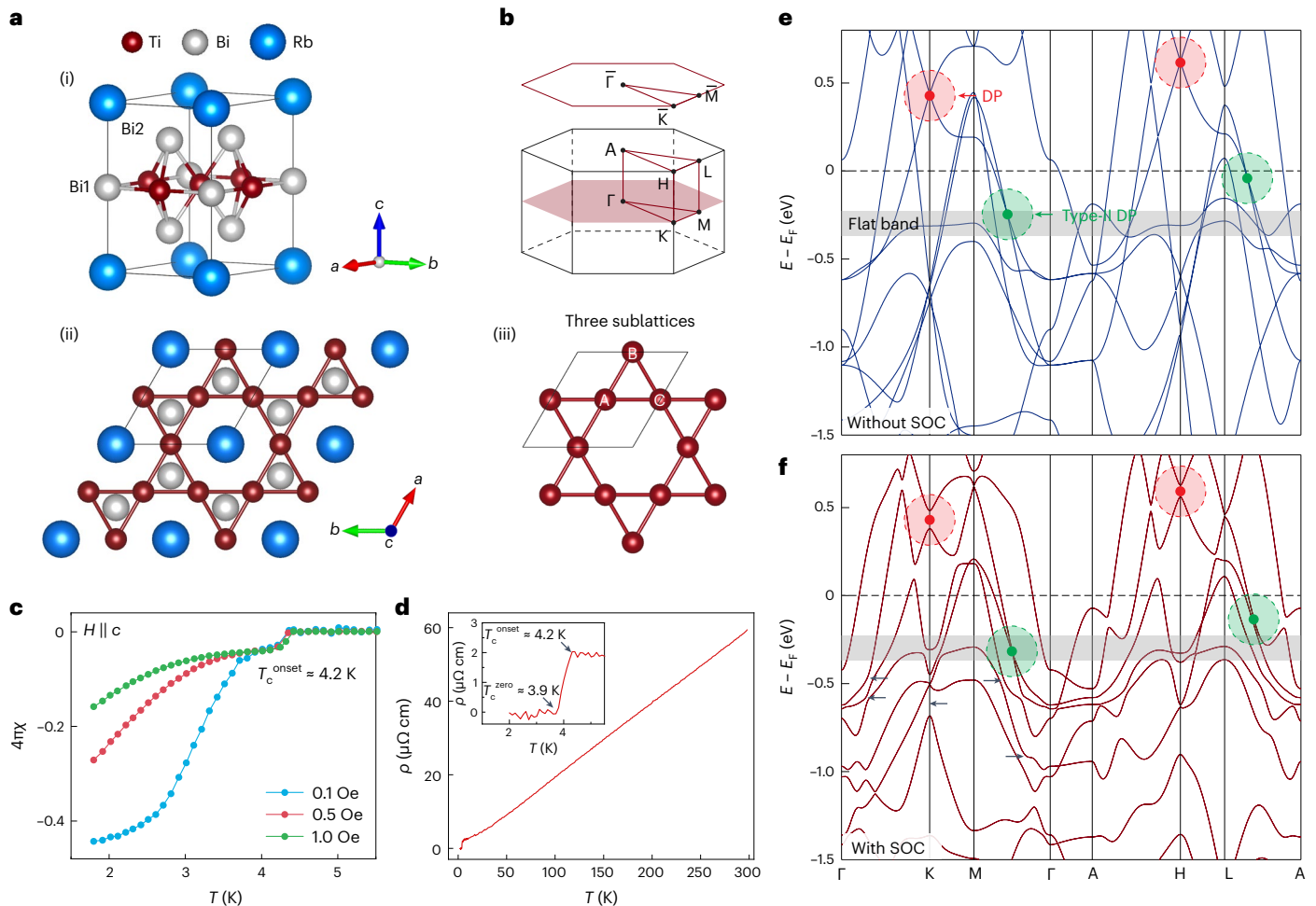


Fig. 1 | Crystal structure and calculated band structure of RbTi_3Bi_5 . **a**, Unit cell of RbTi_3Bi_5 with two types of Bi atoms indicated (i), top view showing the kagome plane (ii) and the three sublattices (referred to as A, B and C) in the kagome lattice (iii). **b**, Bulk BZ of RbTi_3Bi_5 and the projection of the (001) surface BZ. **c**, Magnetic susceptibilities under various magnetic fields for $H \parallel c$, showing the magnetic

shielding effect. **d**, Temperature-dependent resistivity under zero magnetic field. The inset shows the superconducting transition with $T_c^{\text{onset}} \approx 4.2$ K and $T_c^{\text{zero}} \approx 3.9$ K. **e, f**, DFT-calculated electronic structure of RbTi_3Bi_5 without SOC (e) and with SOC (f). The arrows in e and f indicate the DP (red), type-II DP (green) and SOC gap (black). The grey shading highlights the flat band.

vanadium-based superconductors AV_3Sb_5 (where A can be K, Rb or Cs)^{28,29} have attracted much attention recently because they exhibit intriguing similarities to correlated electronic phenomena observed in high-temperature superconductors, such as a pair density wave³⁰, time-reversal symmetry-broken CDW^{31,32} and electronic nematicity³³. However, the nematic order in AV_3Sb_5 is entangled with the CDW, making understanding its origin challenging.

Very recently, a new family of Ti-based kagome metals ATi_3Bi_5 , which are isostructural with AV_3Sb_5 , have been synthesized³⁴. Despite the distinct $3d$ electronic configuration of Ti atoms compared with V atoms, superconductivity occurs at an onset temperature (T_c) of about 4.8 K. The strong spin-orbit coupling (SOC) from Bi atoms can generate intriguing non-trivial topological phenomena. In stark contrast to AV_3Sb_5 , transport measurements on ATi_3Bi_5 show no evidence of a CDW state^{34,35}. Interestingly, an electronic nematicity with rotational symmetry breaking is discovered in the absence of a concomitant translational symmetry breaking^{36,37}, similar to iron-based high-temperature superconductors. Therefore, ATi_3Bi_5 is a tantalizing system for understanding the mechanism behind electronic nematicity and its interplay with intertwined correlated quantum phenomena, such as superconductivity.

In this work, combining high-resolution polarization-dependent angle-resolved photoemission spectroscopy (ARPES) and density

functional theory (DFT) calculations, we systematically investigate the electronic structure of the Ti-based kagome metal RbTi_3Bi_5 . We observe several inter-related topological band features, namely, type-II Dirac nodal lines and non-trivial \mathbb{Z}_2 topological states, as well as characteristic flat bands of the kagome lattices. Remarkably, combined with DFT calculations, our polarization-dependent ARPES measurements reveal the change in orbital character along the $\bar{\Gamma}-\bar{M}$ and $\bar{\Gamma}-\bar{K}$ directions, suggesting a strong intrinsic interorbital coupling in Ti-based kagome metals, reminiscent of iron-based superconductors. Doping-dependent measurements uncover the orbital-selective features in the kagome bands, which is explained by the $d-p$ hybridization. The observed interorbital coupling and $d-p$ hybridization not only account for the electronic nematicity in ATi_3Bi_5 , but also give deeper insights into the origin of nematicity in kagome superconductors. In particular, we show the implications of the intrinsic orbital-bond nematic orders in the kagome lattice and establish ATi_3Bi_5 as an ideal system where electronic nematicity can be studied in its pure form, unperturbed by other intervening orders.

RbTi_3Bi_5 crystallizes in a layered hexagonal lattice consisting of alternately stacked Ti-Bi sheets and Rb layers (Fig. 1a(i),(ii)). It shares the same crystal structure as AV_3Sb_5 , but with a kagome net of Ti atoms replacing V. The corresponding bulk Brillouin zone (BZ) and the projected two-dimensional BZ on the (001) surface are illustrated in

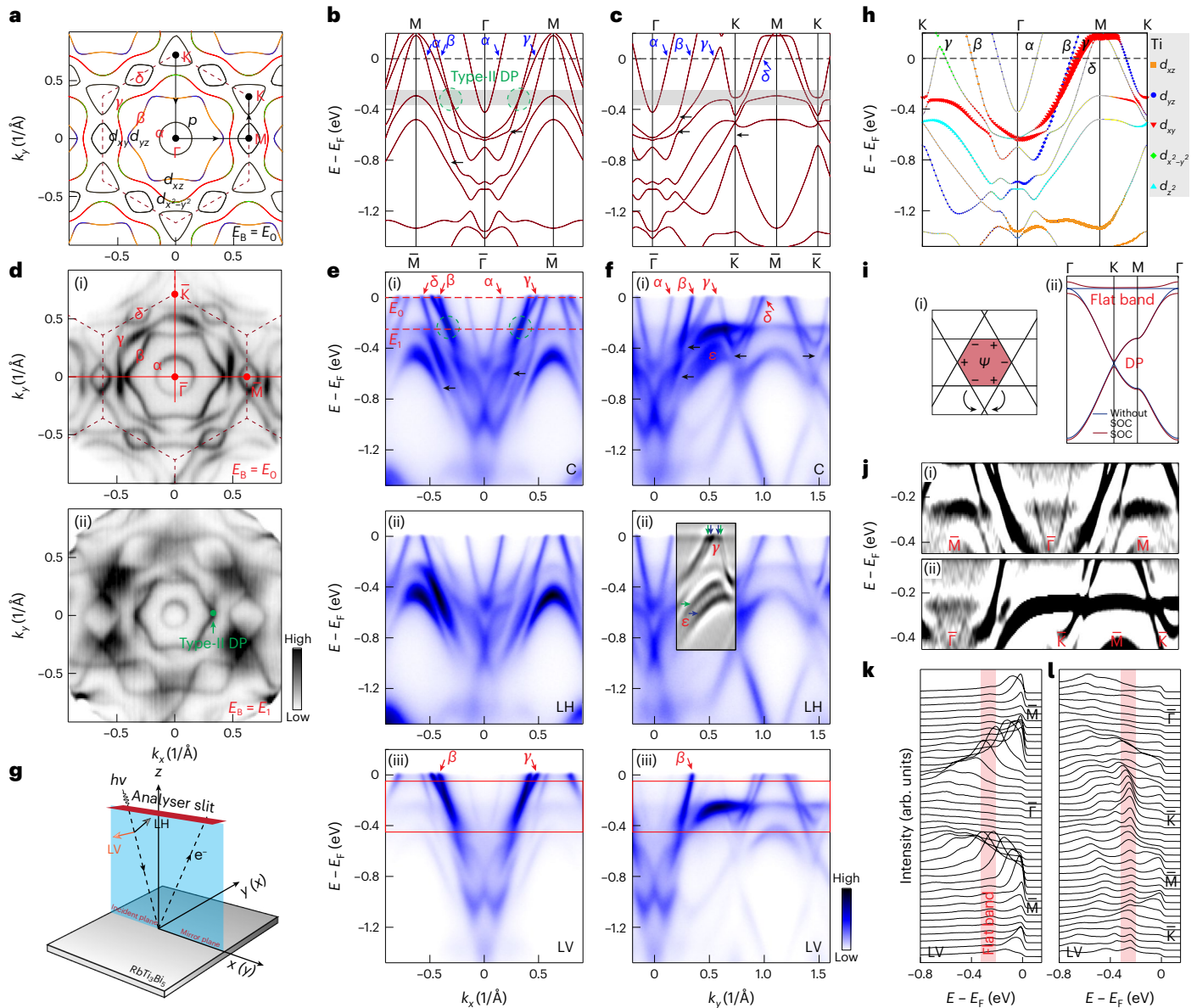


Fig. 2 | Polarization-dependent measurements of the kagome bands.

a, Calculated Fermi surface. The dashed hexagon represents the BZ. **b, c**, DFT band structure along the Γ -M (**b**) and Γ -K (**c**) directions. **d**, Constant-energy contours at the Fermi level (E_F) (i) and flat band (ii). The green arrow in (ii) marks the type-II DP. **e**, ARPES spectra along the Γ -M direction, probed with circularly (C) (i), linear horizontally (LH) (ii) and linear vertically (LV) (iii) polarized light. The red dashed line in (i) marks the energy position of the constant-energy contours in **d, f**. Same data as in **e**, but measured along the Γ -K direction. The second-derivative spectrum as a function of energy is shown as the inset in (ii) to

highlight the band splitting in the γ and ε bands. The black arrow in **b-f** highlights the SOC gap. **g**, Experimental geometry of the polarization-dependent ARPES measurements. **h**, Orbital-resolved DFT band dispersion originating from sublattice A (Fig. 1a(iii)), along the K- Γ -M-K path (black arrow in **a**). **i**, Destructive interference of hopping in the frustrated kagome lattice (i), as well as the expected flat band and DP (ii). **j**, Zoomed-in second-derivative plots with respect to energy of the selected region in **e**(iii) (i) and **f**(iii) (ii), as indicated by the red box in **e** and **f**, respectively. **k**, EDCs of **e**(iii). **l**, EDCs of **f**(iii).

Fig. 1b, with the high-symmetry points indicated. Magnetic susceptibility (Fig. 1c) and resistivity (Fig. 1d) measurements show a superconducting transition in RbTi₃Bi₅ at an onset T_c value of about 4.2 K, which is slightly lower than that in CsTi₃Bi₅ (ref. 36). The band structure of RbTi₃Bi₅ from DFT calculations without/with SOC is displayed in Fig. 1e,f (Fig. 2b,c). The characteristic band feature of the kagome lattice, for example, the flat band, emerges around a binding energy (E_b) of 0.3 eV (Fig. 1e,f, grey-coloured region) and a Dirac point (DP) occurs above the Fermi level (E_F) at the \bar{K} point (Fig. 1e, red arrow and circle). A detailed examination of the band structure of Ti-based kagome metals along the out-of-plane momentum reveals a type-II Dirac nodal line (Figs. 1e,f and 2b, green circle; Supplementary Fig. 1). The type-II nodal

line is protected by a mirror symmetry when the SOC is ignored. With the further inclusion of SOC, a negligible gap opens at the type-II nodal line, distinct from the pronounced gaps that open at the DP at the \bar{K} point (Fig. 1f) and at the trivial band-crossing points (Figs. 1f and 2b,c, black arrows). To gain an insight into the electronic nematicity and search for the non-trivial band topology, we employ polarization-dependent ARPES to systematically study the electronic structure of single-crystal RbTi₃Bi₅.

In Fig. 2d(i), we first present the measured Fermi surface sheets, which consist of one circle-like and two hexagonal-like electron pockets near the zone centre (Γ point), one rhombic-like hole pocket at the zone boundary (M) and one triangle-like electron pocket near the zone

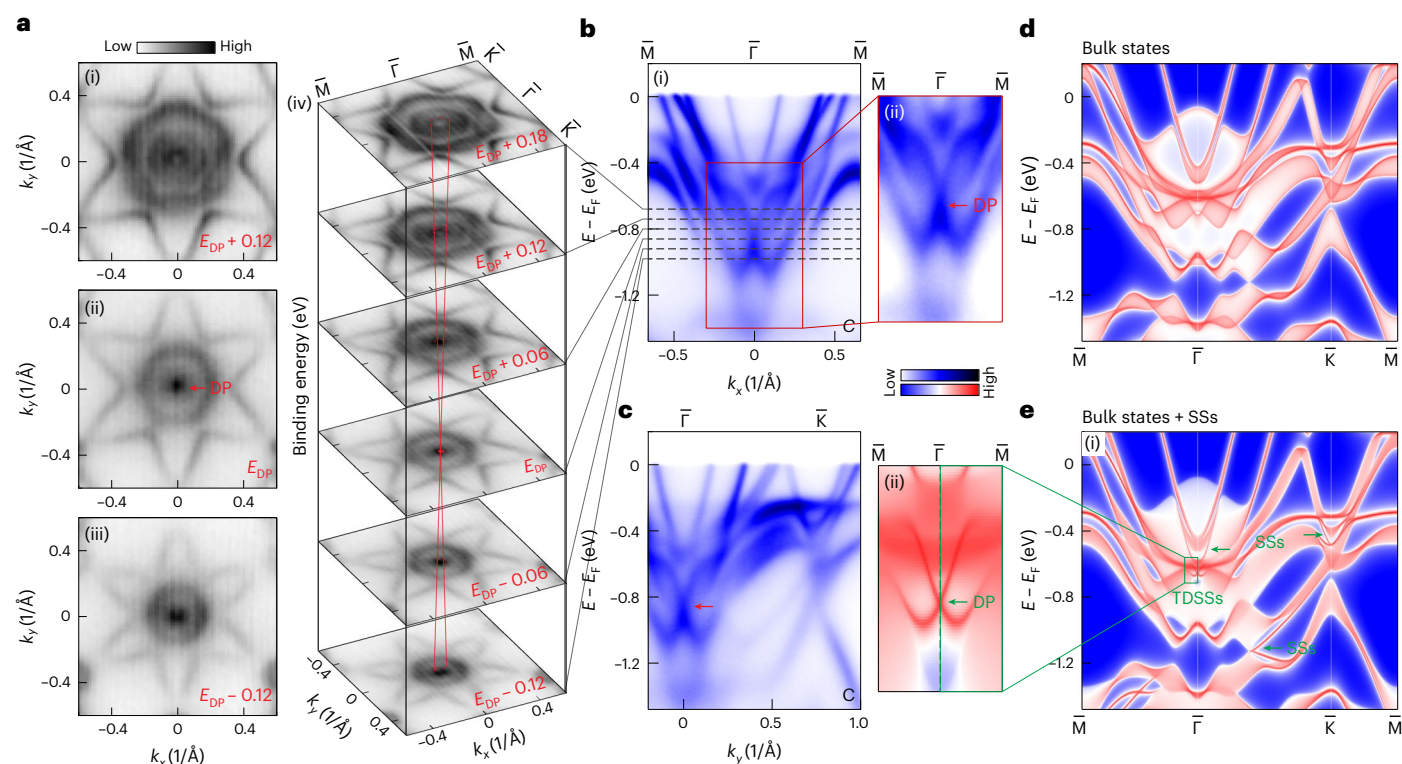


Fig. 3 Z_2 topological surface states in RbTi_3Bi_5 . **a**, Constant-energy contours at +0.12 eV (i), 0 eV (ii) and -0.12 eV (iii) with respect to E_{DP} , as well as the stacking plots (iv). **b**, Experimental band dispersion along the $\bar{\Gamma}$ - \bar{M} direction (i) and an enlarged plot of dispersion near the DP (ii). **c**, Same data as in **b**, but along the $\bar{\Gamma}$ - \bar{K} direction. **d, e**, The (001) surface Green function projection of pure bulk states

(**d**) and the theoretical surface spectra (bulk states and surface states (SSs)) (**e**). Zoomed-in plot of the calculated dispersion (**e(ii)**), revealing the TDSSs shown in **e(ii)**. Besides the TDSSs, the calculations also identify SSs along the $\bar{\Gamma}$ - \bar{K} path (green arrow in **e(ii)**); however, these states may overlap with the bulk states.

corner (\bar{K}), which agree well with the theoretical calculations (Fig. 2a). The dispersive nature of the bands contributing to the Fermi surface is revealed along two representative high-symmetry paths, namely, the $\bar{\Gamma}$ - \bar{M} (Fig. 2e) and $\bar{\Gamma}$ - \bar{K} (Fig. 2f) directions (the four bands crossing E_F are denoted as α , β , γ and δ hereafter). Due to the multi-orbital nature of the Ti d orbitals, ARPES measurements of the band structure are strongly sensitive to photon polarization. In principle, according to the selection rules in photoemission³⁸, the bands can be selectively detected depending on their symmetry with respect to the mirror plane formed by the photon beam, sample and spectrometer (Fig. 2g). By exploiting these selection rules, the bands' characters can be experimentally determined (Supplementary Fig. 2 shows the details of the matrix element analysis under our ARPES geometry). For instance, the β and γ bands are selectively detected by linear vertical (LV) polarization (Fig. 2e(iii)) along the $\bar{\Gamma}$ - \bar{M} direction, indicating an odd symmetry (that is, d_{yz} and d_{xy} orbitals) with respect to the mirror plane; meanwhile, along the $\bar{\Gamma}$ - \bar{K} direction, the β and γ bands are detected by LV polarization (Fig. 2f(iii)) and linear horizontal (LH) polarization (Fig. 2f(ii)), respectively. If the β and γ bands retain their orbital characters along the $\bar{\Gamma}$ - \bar{M} and $\bar{\Gamma}$ - \bar{K} directions, they would—in principle—be assigned to the d_{xy} and d_{yz} orbitals, respectively. However, this apparently contradicts the orbital characters from the theoretical calculation³⁶ (Supplementary Fig. 2). This motivates us to consider the interorbital coupling among the non-degenerate orbitals (d_{yz}/d_{xz} and $d_{xy}/d_{x^2-y^2}$) in the kagome lattice. In Fig. 2h, we show the calculated orbital-resolved band dispersion originating from sublattice A (Fig. 1a(iii)), invariant under mirror reflection M_{xz} and M_{yz} , where the β (γ) bands along the $\bar{\Gamma}$ - \bar{M} and $\bar{\Gamma}$ - \bar{K} directions mainly comprise the d_{yz} (d_{xy}) and d_{xz} ($d_{x^2-y^2}$) orbitals, respectively. The variation in orbital characters along different paths is consistent with the results from the polarization-dependent

measurements (Fig. 2e(ii),(iii),f(ii),(iii) and Supplementary Fig. 2), implying a strong intrinsic interorbital coupling in Ti-based kagome metals.

The experimental band dispersions (Fig. 2e,f) also show good overall agreement with the DFT calculations (Figs. 1f and 2b,c). As shown in Fig. 2e(i),(iii), as E_b increases, the β and γ bands separated at E_F (Fig. 2d(i) and Fig. 2e(i),(iii)) evolve to intersect near $E_b = 0.25$ eV (Fig. 2d(ii) and Fig. 2e(i),(iii)), forming the predicted type-II DP (Fig. 2b and Supplementary Fig. 1). As expected from the destructive interference of hopping in the frustrated kagome lattice (Fig. 2i) and the DFT calculations in RbTi_3Bi_5 (Figs. 1e,f and 2b,c), a strikingly non-dispersive feature near E_F at around $E_b = 0.25$ eV is revealed (Fig. 2e(i),f(i)). Accordingly, as shown in the constant-energy contour at $E_b = E_1$ (Fig. 2d(ii)), the spectral weight of this feature is uniformly distributed almost across the entire two-dimensional momentum space. The flat feature is more evident under LV-polarized light (Fig. 2e(iii),f(iii),j) and further evidenced by the non-dispersive peak in the energy distribution curves (EDCs) (Fig. 2k,l, red-shaded area).

Besides the type-II Dirac nodal line and flat bands, the high resolution in the ARPES measurement allows us to reveal some fine structures in band dispersions. As shown in Fig. 2f(i),(ii), a double-band splitting is observed in the γ and ε bands along the $\bar{\Gamma}$ - \bar{K} path, more clearly revealed in the second-derivative plot (Fig. 2f(ii), arrows). Furthermore, the effect of SOC on band dispersions, that is, the SOC-associated gaps, are directly seen (Fig. 2e(i),f(i), black arrows). Apparently, the DFT-calculated bands with SOC (Fig. 2b,c) can better capture the experimental band structure in RbTi_3Bi_5 (Fig. 2e,f and Supplementary Fig. 3). The prominent SOC promotes the existence of the topologically non-trivial Dirac surface states (TDSSs) predicted by the ab initio calculations^{34,39,40}.

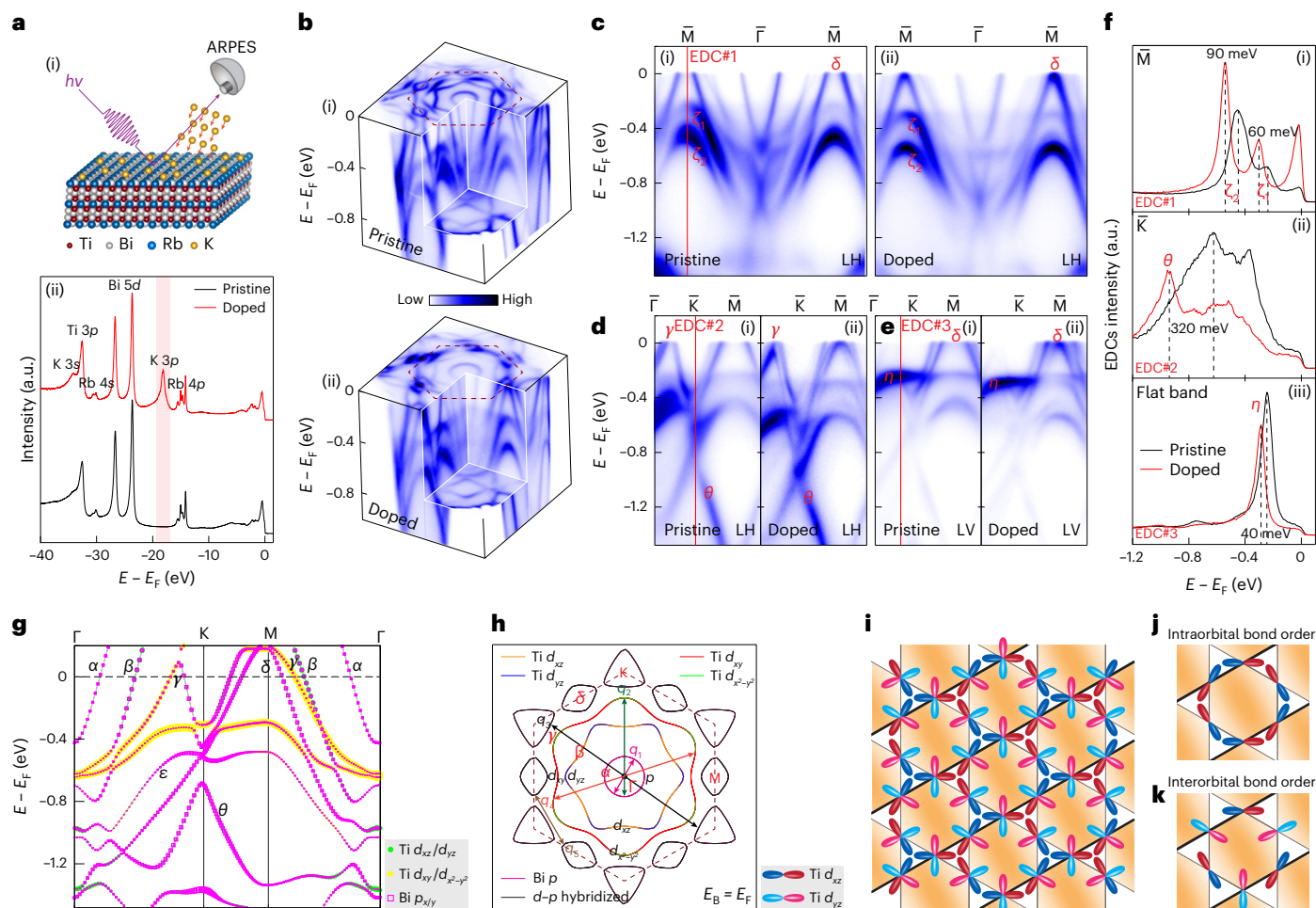


Fig. 4 | Orbital-selective doping effect and d - p hybridization in RbTi_3Bi_5 . **a**, Sketch of in situ K deposition (i) and doping dependence of the core-level photoemission spectrum, showing the characteristic Rb 4s, Bi 5d and Ti 3p peaks (ii). On K deposition, the K 3p peak emerges (red curve), which is absent on the pristine surface (black curve). **b**, Three-dimensional intensity plot of the electronic structure measured on the pristine (i) and K-doped (ii) surfaces. **c**, Doping evolution of the band dispersion along the $\bar{\Gamma}$ - \bar{M} direction measured on the pristine (i) and K-doped (ii) surfaces, probed with LH-polarized light. **d,e**, Same data as in **c**, but measured along the $\bar{\Gamma}$ - \bar{K} direction with LH (**d**) and LV (**e**) polarizations. **f**, Doping-dependent EDCs taken around the M point (i), K point

(ii) and flat band (iii). The momentum location of the EDCs (#1-#3) is marked by the red line in **c-e**, respectively. **g**, Ti d - and Bi p -orbital-resolved DFT band dispersion. **h**, Calculated Fermi surface showing four pockets contributed by different orbital bands. The scattering vectors (q_1 - q_3) are the wavevectors of the quasiparticle interference patterns in scanning tunnelling microscopy/scanning tunnelling spectroscopy measurements³⁶. **i-k**, Interorbital and intraorbital couplings in the Ti-based kagome lattice (**i**), intraorbital band order (**j**) and interorbital band order (**k**). The yellow background in **i-k** represents rotational symmetry breaking.

TDSSs originating from a Z_2 bulk topology are indeed observed in RbTi_3Bi_5 (Fig. 3). A series of experimental constant-energy contours (Fig. 3a), measured from +0.18 to -0.12 eV with respect to E_{DP} (binding energy of the DP), clearly show the evolution of TDSSs in the energy space around the $\bar{\Gamma}$ point. To closely visualize the momentum-space structure of the Dirac bands, we show the band dispersions along two different high-symmetry directions, namely, $\bar{\Gamma}$ - \bar{M} (Fig. 3b) and $\bar{\Gamma}$ - \bar{K} (Fig. 3c). Photon-energy-dependent measurements reveal that Rashba-like bands (Fig. 3b(ii)) around the $\bar{\Gamma}$ point do not disperse with respect to photon energy (and thus, k_z), in contrast to the bulk states (Supplementary Fig. 4), indicating their two-dimensional surface nature. To investigate the topological nature of the Rashba-like feature, we calculated the Z_2 topological invariant of the occupied bands using parity products at all the time-reversal invariant momenta. We found that the TDSSs originate from d - p band inversion around the A point (Supplementary Fig. 4). Figure 3d shows the calculated bulk states projected onto the (001) surface together with the theoretically calculated surface spectra (Fig. 3e(i)). The TDSSs derived from the bulk non-trivial topology

and protected by time-reversal symmetry are theoretically identified around the $\bar{\Gamma}$ point (Fig. 3e(ii)). The shape of TDSSs observed in our experiment (Fig. 3b(ii)) and their connection with the bulk bands are consistent with our theoretical calculations (Fig. 3e(ii) and Supplementary Fig. 4). However, since the energy position and size of the surface states are highly sensitive to the details of the surface environment, the energy position of the DP is deeper in the experiment (Fig. 3b(ii)) than in the calculations (Fig. 3e(ii)).

After characterizing the orbital characters and identifying the rich non-trivial band topology, we now demonstrate the direct manipulation of electronic states via in situ surface potassium (K) deposition (Fig. 4a(i)). As shown in Fig. 4a(ii), the successful introduction of K atoms—doping on the sample surface—is confirmed by measuring the K 3p core level (red curve), which is absent on the pristine surface (black curve). To show the overall doping evolution of the band structure, we display the doping-dependent ARPES spectra in volume plots (Fig. 4b). Remarkably, on doping, the top of the δ band is tuned from well above to below the E_F , as shown in the high-symmetry band dispersions along the $\bar{\Gamma}$ - \bar{M} (Fig. 4c) and $\bar{\Gamma}$ - \bar{K} (Fig. 4d,e) directions. This indicates that a

Lifshitz transition of the Fermi surface driven by the δ band is realized with doping (Fig. 4b and Supplementary Fig. 5). A comparative examination of the EDCs, taken at the \bar{M} point, \bar{K} point and flat band, indicates that the band shift does not shift in a simple, rigid fashion (Fig. 4f); rather, the shift is strongly orbit dependent. Specifically, after doping, the hole-like ζ_1 and ζ_2 bands around the \bar{M} point shift by about 60 and 90 meV (Fig. 4f(i), EDC#1), respectively; the hole-like θ band near the \bar{K} point moves down by 320 meV (Fig. 4f(ii), EDC#2); and the flat band (η) along the $\bar{\Gamma}$ – \bar{K} path only drops by about 40 meV (Fig. 4f(iii), EDC#3).

We next turn to discuss the implication of the observed orbital-selective doping effect on the kagome bands. As the kagome layers are embedded between two Bi layers (Fig. 1a(i)), on surface deposition, the electron doping in the kagome layers is mediated by coupling between the Bi p (Supplementary Fig. 6) and Ti d orbitals. The theoretically calculated orbital-resolved band structure distinguishing Ti d and Bi p orbitals (Fig. 4g) clearly reveals a strong d – p hybridization around E_F in RbTi₃Bi₅. The mirror-even (mirror-odd) $d_{xy}/d_{x^2-y^2}$ (d_{xz}/d_{yz}) orbitals under mirror reflection M_{xy} in the Ti-kagome plane couple with p_{xy} bonding (antibonding) orbitals of honeycomb Bi atoms above and below. Interestingly, d – p coupling along the $\bar{\Gamma}$ – \bar{K} path is stronger than that along the $\bar{\Gamma}$ – \bar{M} one. The bands (θ and electron-like γ) around the \bar{K} point and the hole-like δ band around the \bar{M} point have the strongest d – p coupling, echoing the pronounced energy shifts observed on these bands on surface K deposition (Fig. 4c–f(ii) and Supplementary Fig. 7 describe the simulations). This d – p scenario can also account for the revealed double-band splittings (in the γ and ε bands) along the $\bar{\Gamma}$ – \bar{K} path (Fig. 2f(i),(ii)), one of which could be assigned to the surface band and the other to bulk states (Supplementary Fig. 8). As the exposed honeycomb Bi2 layers (Fig. 1a(i)) experience a surface potential, the surface bands with strong d – p coupling can be split from their corresponding bulk bands, resulting in a double-band splitting.

Reminiscent of our finding, prominent nematic features in the scanning tunnelling microscopy measurement are observed from the intraband scattering between the electron pocket (that is, the γ band with d_{xz}/d_{yz} orbitals) around the \bar{K} point (Fig. 4h, wavevector q_3) and between the $d_{xy}/d_{x^2-y^2}$ electron pocket around the $\bar{\Gamma}$ point (Fig. 4h, wavevector q_4)^{36,37}, and the corresponding quasiparticle interference pattern along $\bar{\Gamma}$ – \bar{K} appears to have stronger C_6 -symmetry-breaking signatures. The electronic states connected by the q_3 and q_4 wavevectors show pronounced d – p coupling (Fig. 4g), suggesting the important role of d – p hybridization in promoting nematicity. Moreover, the quasiparticle interference at q_3 (q_4) involves both intraorbital and interorbital d_{xz}/d_{yz} ($d_{xy}/d_{x^2-y^2}$) scattering. In the kagome lattice with three sublattices, the site symmetry is D_{2h} , and thus, all the five orbitals on each site are non-degenerate. In hexagonal systems, nematicity has a unique three-state Potts character^{41,42}, distinct from the Ising-like features in tetragonal systems. Accordingly, the simplest nematic order to break the C_6 rotational symmetry is an onsite sublattice potential, but it induces a uniform symmetry-breaking feature in momentum space, which is inconsistent with the scanning tunnelling microscopy measurements^{36,37}. Given the observed interorbital coupling (Fig. 2a,e,f,h), an alternative scenario is intra- or interorbital bond order, where a stronger bonding (Fig. 4i–k, thick line) between certain sites breaks the six-fold rotational symmetry but preserves the two-fold rotational symmetry (Fig. 4i–k) (for example, d_{xz}/d_{yz} orbitals). It is expected to display noticeable momentum-dependent nematic features. The effective hopping between d orbitals through Bi p_{xy} orbitals can become nematic once the degeneracy of the p_{xy} orbitals is lifted. Importantly, a strong d – p hybridization can make the Ti 3d orbitals more extended and therefore enhance the non-local Coulomb interaction, which can promote the nematic bond order^{13,43}.

Our ARPES results, combined with DFT calculations, identify a remarkable coexistence of flat bands and non-trivial band topology (that is, type-II Dirac nodal line and non-trivial \mathbb{Z}_2 topology) in the Ti-based kagome superconductor RbTi₃Bi₅. The Ti d orbital contributes

to the type-II nodal lines and flat bands, whereas the \mathbb{Z}_2 bulk topology derived from d – p band inversion gives rise to TDSSs. These observations are closely inter-related through the kagome lattice, and call for future investigations into their topological contributions to transport properties and related potential applications. Remarkably, by exploiting polarization-dependent ARPES, our study reveals an intricate change in orbital character along the $\bar{\Gamma}$ – \bar{M} and $\bar{\Gamma}$ – \bar{K} directions (Fig. 2a,h), implying a strong interorbital coupling in the Ti-based kagome lattice in contrast to AV₃Sb₅ (ref. 19). The emergence of electronic nematicity in the absence of CDW and the presence of interorbital coupling in RbTi₃Bi₅ are reminiscent of iron-based superconductors, where the d_{xz}/d_{yz} orbitals are degenerate in tetragonal systems. However, the two sets of d_{xz}/d_{yz} and $d_{xy}/d_{x^2-y^2}$ orbitals in RbTi₃Bi₅, due to the D_{2h} site symmetry group, are non-degenerate, making the Ti-based kagome metals unique and distinct from iron-based superconductors. Additionally, our doping-dependent measurements directly uncover the orbital-selective characters in the multiorbital kagome system. The revealed d – p hybridization, together with interorbital coupling, provides a qualitative explanation for the electronic nematicity in ATi₃Bi₅. Taken together, our findings demonstrate that RbTi₃Bi₅ is a versatile platform for investigating exotic topological and correlated states, and offer valuable insights into the origin of nematic orders that are present in numerous correlated systems competing with superconductivity.

Online content

Any methods, additional references, Nature Portfolio reporting summaries, source data, extended data, supplementary information, acknowledgements, peer review information; details of author contributions and competing interests; and statements of data and code availability are available at <https://doi.org/10.1038/s41567-023-02215-z>.

References

- Chuang, T.-M. et al. Nematic electronic structure in the ‘parent’ state of the iron-based superconductor Ca(Fe_{1-x}Co_x)₂As₂. *Science* **327**, 181–184 (2010).
- Chu, J.-H. et al. In-plane resistivity anisotropy in an underdoped iron arsenide superconductor. *Science* **329**, 824–826 (2010).
- Chu, J.-H., Kuo, H.-H., Analytis, J. G. & Fisher, I. R. Divergent nematic susceptibility in an iron arsenide superconductor. *Science* **337**, 710–712 (2012).
- Rosenthal, E. P. et al. Visualization of electron nematicity and unidirectional antiferroic fluctuations at high temperatures in NaFeAs. *Nat. Phys.* **10**, 225–232 (2014).
- Kuo, H.-H., Chu, J.-H., Palmstrom, J. C., Kivelson, S. A. & Fisher, I. R. Ubiquitous signatures of nematic quantum criticality in optimally doped Fe-based superconductors. *Science* **352**, 958–962 (2016).
- Ando, Y., Segawa, K., Komiya, S. & Lavrov, A. N. Electrical resistivity anisotropy from self-organized one dimensionality in high-temperature superconductors. *Phys. Rev. Lett.* **88**, 137005 (2002).
- Hinkov, V. et al. Electronic liquid crystal state in the high-temperature superconductor YBa₂Cu₃O_{6.45}. *Science* **319**, 597–600 (2008).
- Lawler, M. J. et al. Intra-unit-cell electronic nematicity of the high- T_c copper-oxide pseudogap states. *Nature* **466**, 347–351 (2010).
- Daou, R. et al. Broken rotational symmetry in the pseudogap phase of a high- T_c superconductor. *Nature* **463**, 519–522 (2010).
- Fernandes, R., Chubukov, A. & Schmalian, J. What drives nematic order in iron-based superconductors? *Nat. Phys.* **10**, 97–104 (2014).
- Keimer, B. et al. From quantum matter to high-temperature superconductivity in copper oxides. *Nature* **518**, 179–186 (2015).
- Kiesel, M. L. & Thomale, R. Sublattice interference in the kagome Hubbard model. *Phys. Rev. B* **86**, 121105(R) (2012).

13. Kiesel, M. L., Platt, C. & Thomale, R. Unconventional Fermi surface instabilities in the kagome Hubbard model. *Phys. Rev. Lett.* **110**, 126405 (2013).
14. Wang, W.-S., Li, Z.-Z., Xiang, Y.-Y. & Wang, Q.-H. Competing electronic orders on kagome lattices at Van Hove filling. *Phys. Rev. B* **87**, 115135 (2013).
15. Yin, J.-X. et al. Negative flat band magnetism in a spin-orbit-coupled correlated kagome magnet. *Nat. Phys.* **15**, 443–448 (2019).
16. Wu, X. et al. Nature of unconventional pairing in the kagome superconductors AV_3Sb_5 . *Phys. Rev. Lett.* **127**, 177001 (2021).
17. Kang, M. et al. Dirac fermions and flat bands in the ideal kagome metal FeSn. *Nat. Mater.* **19**, 163–169 (2020).
18. Kang, M. et al. Twofold Van Hove singularity and origin of charge order in topological kagome superconductor CsV_3Sb_5 . *Nat. Phys.* **18**, 301–308 (2022).
19. Hu, Y. et al. Rich nature of Van Hove singularities in kagome superconductor CsV_3Sb_5 . *Nat. Commun.* **13**, 2220 (2022).
20. Yan, S., Huse, D. A. & White, S. R. Spin-liquid ground state of the $S=1/2$ kagome Heisenberg antiferromagnet. *Science* **332**, 1173–1176 (2011).
21. Han, T.-H. et al. Fractionalized excitations in the spin-liquid state of a kagome-lattice antiferromagnet. *Nature* **492**, 406–410 (2012).
22. Han, T., Chu, S. & Lee, Y. S. Refining the spin Hamiltonian in the spin-1/2 kagome lattice antiferromagnet $ZnCu_3(OH)_6Cl_2$ using single crystals. *Phys. Rev. Lett.* **108**, 157202 (2012).
23. Fu, M., Imai, T., Han, T.-H. & Lee, Y. S. Evidence for a gapped spin-liquid ground state in a kagome Heisenberg antiferromagnet. *Science* **350**, 655–658 (2015).
24. Liu, E. et al. Giant anomalous Hall effect in a ferromagnetic kagome-lattice semimetal. *Nat. Phys.* **14**, 1125–1131 (2018).
25. Morali, N. et al. Fermi-arc diversity on surface terminations of the magnetic Weyl semimetal $Co_3Sn_2S_2$. *Science* **365**, 1286–1291 (2019).
26. Liu, D.-F. et al. Magnetic Weyl semimetal phase in a kagome crystal. *Science* **365**, 1282–1285 (2019).
27. Ko, W.-H., Lee, P. A. & Wen, X.-G. Doped kagome system as exotic superconductor. *Phys. Rev. B* **79**, 214502 (2009).
28. Ortiz, B. R. et al. New kagome prototype materials: discovery of KV_3Sb_5 , RbV_3Sb_5 , and CsV_3Sb_5 . *Phys. Rev. Mater.* **3**, 094407 (2019).
29. Ortiz, B. R. et al. CsV_3Sb_5 : a Z_2 topological kagome metal with a superconducting ground state. *Phys. Rev. Lett.* **125**, 247002 (2020).
30. Chen, H. et al. Roton pair density wave and unconventional strong-coupling superconductivity in a topological kagome metal. *Nature* **559**, 222–228 (2021).
31. Jiang, Y.-X. et al. Discovery of unconventional chiral charge order in kagome superconductor KV_3Sb_5 . *Nat. Mater.* **20**, 1353–1357 (2021).
32. Zhao, H. et al. Cascade of correlated electron states in the kagome superconductor CsV_3Sb_5 . *Nature* **599**, 216–221 (2021).
33. Nie, L. et al. Charge-density-wave-driven electronic nematicity in a kagome superconductor. *Nature* **604**, 59–64 (2022).
34. Yang, H. et al. Titanium-based kagome superconductor $CsTi_3Bi_5$ and topological states. Preprint at <https://arxiv.org/abs/2209.03840> (2022).
35. Werhahn, D. et al. The kagomé metals $RbTi_3Bi_5$ and $CsTi_3Bi_5$. *Z. Naturforsch. B* **77**, 757–764 (2022).
36. Yang, H. et al. Superconductivity and orbital-selective nematic order in a new titanium-based kagome metal $CsTi_3Bi_5$. Preprint at <https://arxiv.org/abs/2211.12264> (2022).
37. Li, H. et al. Electronic nematicity in the absence of charge density waves in a new titanium-based kagome metal. *Nat. Phys.* <https://doi.org/10.1038/s41567-023-02176-3> (2023).
38. Damascelli, A., Hussain, Z. & Shen, Z.-X. Angle-resolved photoemission studies of the cuprate superconductors. *Rev. Mod. Phys.* **75**, 473–541 (2003).
39. Yi, X.-W. et al. Large kagome family candidates with topological superconductivity and charge density waves. *Phys. Rev. B* **106**, L220505 (2022).
40. Jiang, Y. et al. Screening promising CsV_3Sb_5 -like kagome materials from systematic first-principles evaluation. *Chinese Phys. Lett.* **39**, 047402 (2022).
41. Hecher, M. & Schmalian, J. Vestigial nematic order and superconductivity in the doped topological insulator $Cu_xBi_2Se_3$. *npj Quantum Mater.* **3**, 26 (2018).
42. Fernandes, R. M., Orth, P. P. & Schmalian, J. Intertwined vestigial order in quantum materials: nematicity and beyond. *Annu. Rev. Condens. Matter Phys.* **10**, 133–154 (2019).
43. Jiang, K., Hu, J., Ding, H. & Wang, Z. Interatomic Coulomb interaction and electron nematic bond order in FeSe. *Phys. Rev. B* **93**, 115138 (2016).

Publisher's note Springer Nature remains neutral with regard to jurisdictional claims in published maps and institutional affiliations.

Springer Nature or its licensor (e.g. a society or other partner) holds exclusive rights to this article under a publishing agreement with the author(s) or other rightsholder(s); author self-archiving of the accepted manuscript version of this article is solely governed by the terms of such publishing agreement and applicable law.

© The Author(s), under exclusive licence to Springer Nature Limited 2023

¹Photon Science Division, Paul Scherrer Institut, Villigen PSI, Switzerland. ²RIKEN Interdisciplinary Theoretical and Mathematical Sciences (iTHEMS), Wako, Japan. ³Beijing National Center for Condensed Matter Physics and Institute of Physics, Chinese Academy of Sciences, Beijing, People's Republic of China. ⁴School of Physical Sciences, University of Chinese Academy of Sciences, Beijing, People's Republic of China. ⁵Department of Physics, City University of Hong Kong, Kowloon, People's Republic of China. ⁶City University of Hong Kong Shenzhen Research Institute, Shenzhen, People's Republic of China. ⁷Max-Planck-Institut für Festkörperforschung, Stuttgart, Germany. ⁸CAS Key Laboratory of Theoretical Physics, Institute of Theoretical Physics, Chinese Academy of Sciences, Beijing, People's Republic of China. ⁹Center for Correlated Matter and Department of Physics, Zhejiang University, Hangzhou, People's Republic of China. ¹⁰These authors contributed equally: Yong Hu, Congcong Le, Yuhang Zhang. ✉e-mail: yonghphysics@gmail.com; xxwu@itp.ac.cn; hjgao@iphy.ac.cn; ming.shi@psi.ch

Methods

Single-crystal growth and in situ doping

Single crystals of RbTi_3Bi_5 were synthesized using the self-flux method, as reported elsewhere³⁴. Electron doping was achieved by in situ surface K deposition (at 20 K) on RbTi_3Bi_5 samples.

ARPES measurements

The ARPES measurements were carried out at the ULTRA endstation of the Surface/Interface Spectroscopy (SIS) beamline of the Swiss Light Source, using a Scienta Omicron DA30L analyser. The measurements were performed with 64 eV photons and a total energy resolution of 15 meV. The samples were cleaved in situ with a base pressure of better than 5×10^{-11} torr, and measured at 20 K. The Fermi level was determined by measuring polycrystalline Au in electrical contact with the samples.

Computational methods

Band structure calculations were performed by using the method of first-principles DFT as implemented in the Vienna ab initio simulation package code^{44–46}. The Perdew–Burke–Ernzerhof exchange–correlation functional and the projector augmented wave approach are used. Throughout this work, the cutoff energy is set to 500 eV for expanding the wavefunctions into the plane-wave basis, and SOC is included. The BZ is sampled in the k space within the Monkhorst–Pack scheme⁴⁷, and the k mesh used is $9 \times 9 \times 5$ on the basis of the equilibrium structure. We adopt the experimental parameters in the calculation. To get the tight-binding Hamiltonian, we create Wannier functions via the wannier90 package⁴⁸ with a projection of the Bloch states to the atomic orbitals, and then use this Hamiltonian to calculate the surface states using the surface Green function⁴⁹.

Data availability

All data needed to evaluate the conclusions in the paper are present in the paper and/or the Supplementary Information. All other data that support the findings of this study are available from the corresponding authors upon reasonable request. Source data are provided with this paper.

Code availability

The band structures used in this study are available from the corresponding authors upon reasonable request.

References

44. Kresse, G. & Hafner, J. Ab initio molecular dynamics for liquid metals. *Phys. Rev. B* **47**, 558 (1993).
45. Kresse, G. & Furthmüller, J. Efficiency of ab-initio total energy calculations for metals and semiconductors using a plane-wave basis set. *Comput. Mater. Sci.* **6**, 15 (1996).
46. Kresse, G. & Furthmüller, J. Efficient iterative schemes for ab initio total-energy calculations using a plane-wave basis set. *Phys. Rev. B* **54**, 11169 (1996).

47. Monkhorst, H. J. & Pack, J. D. Special points for Brillouin-zone integrations. *Phys. Rev. B* **13**, 5188 (1976).
48. Mostofi, A. A. et al. wannier90: a tool for obtaining maximally-localised Wannier functions. *Comput. Phys. Commun.* **178**, 685 (2008).
49. Lopez Sancho, M. P., Lopez Sancho, J. M., Sancho, J. M. L. & Rubio, J. Highly convergent schemes for the calculation of bulk and surface Green functions. *J. Phys. F: Met. Phys.* **15**, 851 (1985).

Acknowledgements

Work at the Paul Scherrer Institut was supported by the Swiss National Science Foundation under grant no. 200021_188413. X.W. was supported by the National Natural Science Foundation of China (grant no. 12047503). J.M. was supported by the Research Grants Council of Hong Kong via Early Career Scheme (21304023), the Collaborative Research Fund (C6033-22G), the Collaborative Research Equipment Grant (C1018-22E) and the National Natural Science Foundation of China (12104379). J.H. was supported by the Ministry of Science and Technology (grant no. 2022YFA1403901), the National Natural Science Foundation of China (grant no. NSFC-11888101) and the New Cornerstone Foundation.

Author contributions

Y.H. and M.S. conceived the ARPES experiments. Z.Z. grew and characterized the crystals with guidance from H.C., H.Y. and H.-J.G. X.W. and C.L. performed the theoretical calculations and analysis with support from A.P.S. and J.H. Y.H. performed the ARPES experiments with help from J.M., M.R. and M.S. Y.Z. and J.L. performed the transport measurements with guidance from X.D. N.C.P. maintained the ARPES facilities at ULTRA, SIS. Y.H. analysed the data. Y.H. and X.W. wrote the paper with inputs from all authors.

Competing interests

The authors declare no competing interests.

Additional information

Supplementary information The online version contains supplementary material available at <https://doi.org/10.1038/s41567-023-02215-z>.

Correspondence and requests for materials should be addressed to Yong Hu, Xianxin Wu, Hong-Jun Gao or Ming Shi.

Peer review information *Nature Physics* thanks the anonymous reviewers for their contribution to the peer review of this work.

Reprints and permissions information is available at www.nature.com/reprints.